

An Experimentally Validated Combined Stiffness Formulation for a Finite Domain Considering Volume Fraction, Shape, Orientation, and Location of a Single Inclusion

Ilige Hage

*Department of Mechanical Engineering
Notre Dame University-Louaize, Zouk Mosbeh
P. O. Box 72, Zouk Mikael, Lebanon
ilige.hage@ndu.edu.lb*

Ramsey F. Hamade*

*Department of Mechanical Engineering
American University of Beirut, Riad El-Solh
Beirut 1107 2020, Lebanon
rh13@aub.edu.lb*

Received 22 September 2017

Accepted 07 January 2018

Published 7 February 2018

This work characterizes the stiffness of a finite domain containing one (biaxial ellipsoidal) void due to the combined effect of inclusion's attributes: (1) size or volume fraction, VF, (2) shape or aspect ratio, AR, (3) angular orientation, and (4) location (position) within the matrix. The values and ranges of these ellipsoidal inclusion attributes are varied according to a matrix developed using design of experiments (DOE). Modified Mori-Tanaka method combined with dual-eigenstrain method (interior and exterior eigenstrain methods) is used to determine the effective stiffness tensor of the composite domain. Employing the numerically calculated normalized axial modulus E_{11}/E_m values in SAS/STAT®, a nonlinear mathematical expression of E_{11}/E_m as function of the void's variables is arrived at Stiffness values found from the numerical homogenization scheme are experimentally corroborated using compression tests conducted on 3D-printed ABS cubes having a single ellipsoidal inclusion of various geometric attributes. In addition, finite element simulations were run of said uniaxial compression test cases to further validate the numerical homogenization results. Corroborated findings suggest that while the location of the inclusions in the matrix have no significant effect on normalized modulus E_{11}/E_m , the void's volume fraction has the largest effect where it decreases with VF. The effect of the void's orientation and elliptical aspect ratio are significant. E_{11}/E_m increases with AR at angles ranging from 0–30°; at 45° E_{11}/E_m are almost constant

*Corresponding author.

with AR, at angles of 60–90° values of E_{11}/E_m decrease with AR. As AR approaches unity, the effect of orientation decreases significantly.

Keywords: Composite; homogenization; effective stiffness; Eshelby tensor; FEM.

1. Introduction

Determining the elastic properties of materials due to inclusions has long been of interest with cases such as circular holes in 2D space having been studied early in the classical mechanics literature (e.g., Timoshenko *et al.* [1951]). By way of calculating the eigenstrains, [Eshelby, 1957] determined, in what is referred to as a self-consistent scheme, the elastic constants of an ellipsoidal (oblate spheroid) inclusion. Mori and Tanaka [1973], based on the equivalent inclusion work of Eshelby, developed an effective field approximation for inhomogeneity in infinite medium by averaging the stress field.

In developing homogenization schemes, a dual eigenstrain method proposed by Zhong and Meguid [1996, 1999] and Li *et al.* [2007a,b] prescribed an eigenstrain field in both the interior and exterior regions of the inclusion simultaneously. Yu and Tang [2010] developed a micromechanics model (the variational asymptotic method for unit cell homogenization (VAMUCH)) to predict the effective properties of periodically heterogeneous materials and recover the local fields. Anouar *et al.* [2010] and Sun *et al.* [2017] have used Finite element method with classical homogenization schemes to predict elastic properties of composites. By using Eshelby's eigenstrain method and the Mori–Tanaka averaging scheme, Ma and Gao [2014] obtained effective stiffness tensor based on a simplified strain gradient elasticity theory (SSGET). An inclusion is defined as a subdomain Ω_I in an infinite domain Ω_∞ , where a stress-free eigenstrain ε^* is prescribed in the inclusion Ω_I and vanishes outside.

With the advent of composite materials, much micromechanics-based work has since been reported on determining effective elastic moduli of three-dimensional (3D) matrix with inclusions. Early works include that of Weng [1984] reporting on spherical inclusions and Huang and Chandra [1994] reporting on distributed cracks. Tandon and Weng [1984] examined the influence of inclusions' aspect ratio (from zero to infinity) on the effective elastic moduli of composite with spheroidal and unidirectionally aligned inclusions using Mori–Tanaka's theory. A generic histogram based on the numerical expression for the average tensor (S) in Eshelby's equivalent inclusion method of internal stress determination in composite materials is used by Johannesson and Pedersen [1998] to obtain upper and lower bound estimates of the effective properties and internal stresses of thermo-mechanical transversely isotropic fiber composites with different aspect ratios and orientations. Marklund *et al.* [2008] reported on the effect of constituent properties, and geometrical parameters (fiber aspect ratio and orientation) on effective properties of wood fiber composites was determined using the micro-mechanical model extension of

Hashin's formulations. Krzhechkovskii [1979] considered the elastic and strength characteristics of composite materials based on hollow spherical inclusions. An application involving a Mori–Tanaka homogenization scheme was studied by Rouhi and Rais-Rohani [2011] whereby the variation of the Young's modulus of the CNF enhanced vinyl ester as a function of CNF aspect ratio for different volume fractions. A study of the mechanical and thermo-mechanical effective properties using Mori–Tanaka of carbon nano-tube (CNT) reinforced nano-composites is presented by Dong [2014] to describe the effects of CNT aspect ratio and orientation. The effect of shape is also considered by Yan *et al.* [2010] where one elliptical inclusion is modeled with several aspect ratios.

To the authors' best knowledge, no homogenization work has been reported on the combined effect of inclusion location (position) within the representative volume element (RVE) or relating the effect of the four combined variables (volume fraction, aspect ratio, orientation, and location) to the finite domain's stiffness in one formulation. Therefore, we develop in this work a deterministically-based procedure that applies dual eigenstrain method similar to that of Li *et al.* [2007a,b] while taking into account the combined influence of the inclusion's volume fraction, shape, orientation, and location in the matrix. We enhance the methodology proposed by Li *et al.* [2007b] while considering one case of an inclusion at the center of the RVE with its coordinate system aligned with the major axis of the inclusion. Numerous other scenarios are considered with an inclusion of different volume fractions, ellipsoidal shapes, orientations, and locations in the matrix.

Utilizing this homogenization methodology, the effective stiffness tensors of these cases are determined numerically (MATLAB®) as a function of the ellipsoidal inclusion's attributes due to the complexity of the tensor calculations and the numerous input variables. Derived then are normalized longitudinal Young's modulus (with respect to matrix) values, E_{11}/E_m . To obtain faster approximate solutions for this homogenization methodology, numerical solution values were fed into a nonlinear regression module in SAS/STAT® that resulted in an equation that returns E_{11}/E_m as function of the four inclusion variables: volume fraction, ellipsoidal aspect ratio, orientation, and location. Numerical solutions were verified with experimental compression tests. Design of experiments (DOE) software SAS/JMP® is used to design a matrix of test cubes perforated by one ellipsoidal inclusion with VF values ranging from 0 to 0.5, aspect ratio (minor/major axis length) from 0.1 to 1, orientation (from normal to the Cartesian system's 1 direction (0°) to parallel to it (90°) in increments of 15°), and location within cube (offset from cube's center along the diagonal). Said cubes were 3D printed from ABS (Visjet®) material. For each test case, effective stiffness values were measured in compression mode using a universal testing machine as determined from the linear elastic portion of the experimental curves. Last, FEM (DEFORM®) estimates of stiffness values were obtained for said test cubes. Normalized stiffness values determined from analytical, numerical, and nonlinear regression model solutions as well as experimental

uniaxial compression tests and FEM were co-plotted and were found to compare well.

2. Homogenization Scheme

In this section, we utilize a scheme based on the modified Mori–Tanaka method combined with dual-eigenstrain method (interior and exterior eigenstrain methods) to determine the combined effective stiffness tensor of the domain. From the dual eigenstrain method, an Eshelby tensor dependent on the inclusion’s shape and position is deduced. Eshelby tensors are re-oriented using a transformation matrix to transfer from a local coordinate system aligned with the major/minor axis of the inclusion to that of the universal global coordinate system.

2.1. Dual eigenstrain

Eshelby showed that if a uniform eigenstrain ε^* is prescribed inside an ellipsoidal inclusion, then the disturbed strain ε^d is related to ε^* by [Eshelby, 1957]

$$\varepsilon^d = S : \varepsilon^*, \tag{1}$$

where S_{ijkl} is a fourth-order tensor (Eshelby tensor). For coordinate points inside the inclusion, the internal deformation field is homogeneous (constant with respect to position). The strain inside the inclusion is given [Ju and Sun, 1999] by

$$\varepsilon = \varepsilon^0 + S^I : \varepsilon^*, \tag{2}$$

where ε^0 is the remote strain and S^I is the fourth-order interior Eshelby tensor. In the case of dual Eigenstrain method proposed by Li *et al.* [2007b], an eigenstrain field is prescribed for both interior and exterior regions of the inclusion simultaneously

$$\varepsilon^*(r) = \begin{cases} \varepsilon_I^*, & \forall r \in \Omega_I, \\ \varepsilon_E^*, & \forall r \in \Omega_E, \end{cases} \tag{3}$$

where Ω_I is the inclusion subdomain (interior) and Ω_E is the domain outside the inclusion (exterior). The disturbance strain field ε^d is the superposition of the disturbance strain field due to the interior eigenstrain and the disturbance strain field due to the exterior eigenstrain field

$$\varepsilon^d(r) = \begin{cases} S^{I,*} : \varepsilon_I^* + S^{-I,*} : \varepsilon_E^*, & \forall r \in \Omega_I, \\ S^{E,*} : \varepsilon_I^* + S^{-E,*} : \varepsilon_E^*, & \forall r \in \Omega_E, \end{cases} \tag{4}$$

where $S^{\cdot,*}$ is the interior (I) eigenstrain finite Eshelby tensor and $\bar{S}^{\cdot,*}$ is the exterior (E) eigenstrain Eshelby tensor. For the external field (points outside of the inclusion) strain varies with position as [Ju and Sun, 1999]

$$\varepsilon(r) = \varepsilon^0 + S^E(r) : \varepsilon^*, \tag{5}$$

where r is position vector from the center of the inclusion, $S^E(r)$ is fourth-order exterior Eshelby tensor (function of the ellipsoid geometry, Poisson’s ratio of the

matrix, and the coordinate position vector). Li *et al.* [2007b] estimated the strain field generated by a single inclusion where the center of inclusion matches the origin of the Cartesian coordinate system of the representative volume element (RVE) and the inclusion axes are aligned with the RVE's Cartesian coordinate system.

This work considers an inclusion taking on different elliptical shapes, volume fractions, offset from the center of the universe, and oriented at different angles. Each inclusion is treated as a subdomain in an infinite domain where a stress-free eigenstrain is prescribed inside the inclusion and vanishes outside. Afterwards, the inclusion is considered inside the bounded RVE, thus an exterior Eshelby is calculated between the inclusion and its boundary. The Eshelby tensor for one inclusion is calculated using the summation of the interior classical Eshelby tensor and exterior Eshelby function of the position. The equations related to the Eshelby tensor comprise two components: one is uniform but is a function of the matrix Poisson's ratio, shape, and orientation and constant with position and the other is a function of the matrix Poisson's ratio, shape, orientation and the re-oriented coordinate vector position. The strain field calculation is estimated with respect to the RVE's Cartesian coordinate using rotation transformation matrix and translation transformation matrix applied to the vector coordinates position (r) of the inclusion (described in subsequent sections) that takes into account the 3D orientation of the inclusion and its location within the RVE.

2.2. Rotation transformation from local to global coordinates

To account for the inclusion orientation, a 3D RVE with its corresponding Cartesian coordinate system is established. The corresponding rotation angles are identified with respect to the RVE Cartesian coordinate. A transformation matrix is utilized to account for the orientation of the inclusion within the RVE and is utilized to transform from the inclusion local coordinate system to the RVE global coordinate system. The local coordinate position vector (primed) may be transformed to the global coordinate position vector of the inclusion (Fig. 1) where \mathbf{N} is a normal vector to plane ($x_1 x_2$)

$$Q_{ij} = Rx1(\theta) * Rx2(\varphi) * Rx3(\gamma)$$

$$= \begin{bmatrix} 1 & 0 & 0 \\ 0 & \cos \theta & -\sin \theta \\ 0 & \sin \theta & \cos \theta \end{bmatrix} * \begin{bmatrix} \cos \varphi & 0 & \sin \varphi \\ 0 & 1 & 0 \\ -\sin \varphi & 0 & \cos \varphi \end{bmatrix} * \begin{bmatrix} \cos \gamma & -\sin \gamma & 0 \\ \sin \gamma & \cos \gamma & 0 \\ 0 & 0 & 1 \end{bmatrix}, \quad (6)$$

$$\begin{bmatrix} x_1 \\ x_2 \\ x_3 \end{bmatrix} = Q_{ij} \begin{bmatrix} x'_1 \\ x'_2 \\ x'_3 \end{bmatrix}, \quad (7)$$

where Q_{ij} is the transformation matrix, θ , φ , and γ are inclusion deviation angles of the primed axis from the global system axis x_1, x_2 , and x_3 .

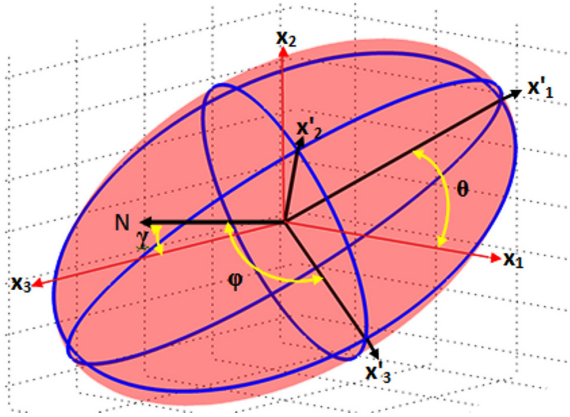


Fig. 1. Ellipsoid with aligned primed axis deviated from the global system axis.

2.3. Re-formulated position vector

The composite is considered as universe Ω_u having one inclusion (domain Ω_I) as seen in Fig. 2, where O_u is the origin of the coordinate system $[x_{1u}, x_{2u}, x_{3u}]$ at the center of the universe.

The origin of the inclusion domain Ω_I is labeled $O_I(x^{(1)} = (x_1^{(1)}, x_2^{(1)}, x_3^{(1)}))$. The inclusion origin's coordinates $(x_1^{(1)}, x_2^{(1)}, x_3^{(1)})$ are obtained with respect to the origin of the universe domain coordinate system Ω_u . The position vector between the subject point P in the universe domain and the origin of the studied inclusion is labeled r and is a function of the orientation and the coordinates of the center of the inclusion (with respect to the origin of the universe domain) $r = f(\theta, \varphi, \gamma, O_I)$. Using the transformation matrix, the coordinate position vector is re-oriented to

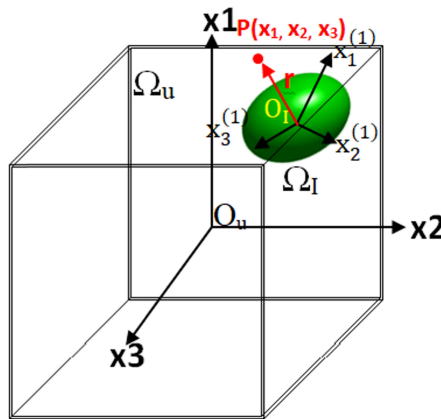


Fig. 2. Illustration of the composite universe.

The effective stiffness tensor expression in [Li *et al.*, 2007b] for one centered inclusion at 0° orientation is reformulated here to be applicable for one inclusion having pre-defined orientation and location in the matrix as

$$\begin{aligned} \bar{C} &= [fC^I : Q_{ijkl} : A_E + (1 - f)C^E : Q_{ijkl} : A_I] \\ &: [f * Q_{ijkl} : A_E + (1 - f) * Q_{ijkl} : A_I]^{-1}, \end{aligned} \tag{11}$$

$$A_E = I^s - \tilde{C}^{-1} : (\tilde{C} - C^E) : \Delta S^*, \tag{12}$$

$$A_I = I^s - \tilde{C}^{-1} : (\tilde{C} - C^I) : \Delta S^*, \tag{13}$$

$$\Delta S_i^* = \langle S_i^{I,*}(\tilde{C}_i, f = f_i) \rangle_{\omega_I} - \langle S_i^{E,*}(\tilde{C}_i, f = f_i) \rangle_{\omega_E}, \tag{14}$$

$$\langle \dots \rangle_{\Omega_u} = \frac{1}{|\Omega_u|_{\Omega_u}} \int_{\Omega_u} \dots \dots d\Omega_u \tag{15}$$

Note that

$$\tilde{C} = aC^1 + (1 - a)C^E, \quad 0 \leq a \leq 1, \tag{16}$$

where

\tilde{C} is the stiffness tensor of the comparison solid,

\bar{C} is the effective stiffness tensor of the composite,

f is the volume fraction,

C^E is the stiffness tensor of the matrix,

C^I is the stiffness tensor of the inclusion,

A^I is the interior strain concentration tensor,

A^E is the exterior strain concentration tensor,

I^S is the identity tensor,

ΔS_i^* is the difference between interior and exterior Eshelby tensors calculated for each inclusion.

As “ a ” is a parameter used to describe the comparison solid, it has to be chosen either to yield $\tilde{C} = C^E$ or $\tilde{C} = C^I$ where the method would degenerate either to interior homogenization or exterior homogenization, respectively. In this work, the parameter “ a ” is set to 0.01. The closed form solutions of interior and exterior Eshelby tensors for various shapes are obtained from [Ma and Gao, 2014; Lu *et al.*, 2013; Ju and Sun, 2001]. Since A^E is function of averaged interior S^I and exterior Eshelby $S^E(r)$ is dubbed as $S(r)$ and \tilde{C}, C^E, C^I therefore $A^E = g(S(r)\tilde{C}, C^E, C^I)$ and $A^I = g'(S(r), \tilde{C}, C^E, C^I)$. Given that $r = f(\theta, \varphi, \gamma, O_D^n)$, the effective stiffness tensor is now a function of all four variables: volume fraction, aspect ratio (inside the Eshelby expression), position, and 3D orientation $(\theta, \varphi, \gamma)$ as

$$\begin{aligned} \bar{C} &= [fC^I : g[S(f(\theta, \varphi, \gamma, O_D^n)), \tilde{C}, C^E, C^I] \\ &+ (1 - f)C^E : g'[S(f(\theta, \varphi, \gamma, O_D^n)r), \tilde{C}, C^E, C^I]] \\ &: [fg[S(f(\theta, \varphi, \gamma, O_D^n)), \tilde{C}, C^E, C^I] \\ &+ (1 - f)g'[S(f(\theta, \varphi, \gamma, O_D^n)r), \tilde{C}, C^E, C^I]]^{-1}. \end{aligned} \tag{17}$$

Hereafter, the solution of the homogenization Eq. (17) is automated using a custom MATLAB® code. Cube with dimensions (size of the universe) of $16 * 16 * 16 \text{ mm}^3$ enclosing one inclusion is considered. The effective stiffness tensors are determined numerically whereby the values for the normalized Young's modulus with respect to that of the matrix (E_{11}/E_m) are calculated. The inclusion's volume fraction, aspect ratio, orientation, and location are considered as independent input variables.

3. Nonlinear Regression Modeling

Considering the long run times required to obtain the homogenization solution (Eq. (17)), it is desirable to obtain an expression that returns comparable values for normalized axial Young's modulus as a function of the four variables as $E_{11}/E_m = f(\text{VF}, \text{AR}, l, \gamma)$ where l is the inclusion location and γ is the inclusion rotation angle with respect to axis x_3 . Numerical results for all 805 cases obtained using the homogenization methodology are used as input for SAS/STAT® software (procedure "PROC MODEL") to develop such an expression. The output is a nonlinear model that best fits these numerical results. Several predictive models were tested with best model obtained based on maximizing R squared values when comparing the results of fitting the regression model to the values calculated from Eq. (17)

$$\begin{aligned} \frac{E_{11}}{E_m} = & a1 + a2 * \gamma + a3 * vf^3 + a4 * ar^{\frac{1}{2}} + a5 * l + a6 * vf * ar \\ & + a7 * vf * \gamma + a8 * vf * l + a9 * ar * \gamma + a10 * ar * l + a11 * l * \gamma \\ & + a12 * vf * ar * \gamma + a13 * vf * ar * \gamma * l. \end{aligned} \quad (18)$$

The 13 coefficients listed in Eq. (18), labeled a1–a13, are identified using the nonlinear modeling Gauss method in SAS/STAT® with 805 observations and convergence criteria. Retaining only the statistically significant terms (having p -values < 0.05) yielded the expression

$$\begin{aligned} \frac{E_{11}}{E_m} = & 0.405642 + 0.347302 * \gamma + 0.430649 * vf^3 + 0.559994 * ar^{\frac{1}{2}} + 0.053014 * l \\ & - 1.64173 * vf * ar - 1.43225 * vf * \gamma - 0.19414 * vf * l - 0.36156 * ar * \gamma \\ & - 0.0345 * l * \gamma + 1.671703 * vf * ar * \gamma + 0.09702 * vf * ar * \gamma * l. \end{aligned} \quad (19)$$

4. Validation: Experimental Compression Testing

In this section, experimental validation of the scheme culminating in Eq. (17) (and the associated SAS-fitted Eq. (19)) was sought via mechanical compression tests performed on 3D printed cubes (ABS crystal plastic material from VisiJet®) and finite elements method, respectively. Each experiment is repeated three times

by printing each case cube three times (results obtained from compression tests are almost identical and the values reported below are the corresponding average values).

4.1. Design of experiments

Several test cases of the cube universe are developed using DOE SAS/JMP® software to determine the effect of inclusion’s volume fraction, orientation, shape, and location in the matrix on the effective Young’s modulus of the composite. By identifying parameters (and their variations) that affect the test results, full factorial DOE matrix is developed with four variables (Table 1).

Based on the number of variables and their levels, the total expected number of cases is $12 * 3 * 14 * 7 = 3528$ for a full-factorial study. This number is reduced for each of the three locations by adding a constraint to ensure that the inclusion is within the boundaries of the universe domain (cube) as follows:

(1) Location 0 mm (0,0,0) (385 cases covering VF = [0.05; 0.1; 0.2; 0.25; 0.3; 0.35; 0.4; 0.5]; AR = [0.1; 0.2; 0.3; 0.4; 0.5; 0.55; 0.65; 0.7; 0.75; 0.8; 0.9; 1]; orientation = [0°; 15°; 30°; 45°; 60°; 75°; 90°]);

(2) Location 1 mm (1,1,1) (238 cases covering VF = [0.05; 0.1; 0.2; 0.25; 0.3; 0.35]; AR = [0.2; 0.3; 0.4; 0.5; 0.55; 0.65; 0.7; 0.75; 0.8; 0.9; 1]; orientation = [0°; 15°; 30°; 45°; 60°; 75°; 90°])

(3) Location 1.5 mm (1.5,1.5,1.5) (182 cases covering VF = [0.05; 0.1; 0.2; 0.25]; AR = [0.1; 0.2; 0.3; 0.4; 0.5; 0.55; 0.65; 0.7; 0.75; 0.8; 0.9; 1]; orientation = [0°; 15°; 30°; 45°; 60°; 75°; 90°]).

Consequently, the total number of numerical cases was reduced to 805. The size of the universe is set as $16 * 16 * 16 \text{ mm}^3$. Inclusion’s volume fraction, aspect ratio, orientation, and location are considered as inputs for each of these 805 cases.

The composite is designed to have the same matrix properties as the ABS material used in 3D printing (Sec. 4.2) with compressive Young’s modulus $E_m = 0.635 \text{ GPa}$ and matrix Poisson’s ratio $\nu_m = 0.35$ (determined experimentally using uniaxial compression test which was done on the directions 1, 2 and 3 of the solid cube, were the results are quite the same proving an isotropic matrix, and the average value for the three directions is reported).

The inclusions are considered to be voids ($E_i = 0 \text{ GPa}$, $\nu_i = 0$). The mechanical properties of the matrix and the void inclusion are listed in Table 2.

Table 1. DOE test matrix with variables and levels.

Variable	Levels	
1. Shape (Aspect ratio)	12 cases	0.1;0.2;0.3;0.4;0.5;0.55;0.65;0.7;0.75;0.8;0.9;1
2. Location (coordinates in mm)	3 cases	0 for (0,0,0); 1 for (1,1,1); 1.5 for (1.5,1.5,1.5)
3. Volume fraction	14 cases	0;0.05;0.1;0.2;0.25;0.3;0.35;0.4;0.5;0.6;0.7;0.8;0.9;1
4. Orientation	7 cases	0°; 15°; 30°; 45°; 60°; 75°; 90°

Table 2. Mechanical properties of matrix and inclusion.

Entity	Young's modulus (GPa)	Poisson's ratio
Matrix	0.635	0.35
Inclusion	0	0

4.2. Compression testing

In order to generate test specimens with predefined inclusion's shape, size, orientation, and location, 3D printing is employed using a professional 3D printer ProJet® 3510 HD (printing ABS VisiJet® M3 Crystal material). The size of the standard cube universe is $16 * 16 * 16 \text{ mm}^3$. One constraint that resulted in excluding some test cases was to keep only the cases with combined inclusion variables that would result in the inclusion fitting well within the cube domain. This realistic requirement resulted in retaining three locations, four orientations, six volume fractions (maximum = 0.5), and six aspect ratios that were sufficient to test all of the four variables. To further reduce the number of tests to a reasonable number, the Taguchi orthogonal array method was employed to produce a partial factorial test matrix. This method is typically used in experiments to study the effect of several factors and uses a set of arrays called orthogonal arrays that produces a minimum number of experiments yet retaining full information of all the factors that affect the performance parameter. Consequently, the number of tests was reduced from full factorial (805 cases) to 86 cases:

(1) Location = 0 mm (0,0,0): 66 cases covering VF = [0.1; 0.2; 0.3; 0.35; 0.4; 0.5]; AR = [0.2; 0.4; 0.65; 0.75; 0.9; 1]; orientation = [0°; 30°; 60°; 90°]

(2) Location = 1 mm (1,1,1): 12 cases covering VF = [0.1; 0.2; 0.3; 0.35]; AR = [0.4; 0.65; 0.75; 0.9; 1]; orientation = [0°]

(3) Location = 1.5 mm (1.5,1.5,1.5): 8 cases covering VF = [0.1; 0.2]; AR = [0.4; 0.65; 0.75; 0.9; 1]; orientation = [0°].

In preparation for printing, Cubify Design® software was used to generate *.stl files of dimensional tolerance of 0.001 mm. The printed cubes were labeled with corresponding case numbers. Shown in Fig. 3 are four examples of printed cubes: cube 1 at Location = 0, VF = 0.1, AR = 0.75, angle = 30; cube 2 at Location = 0, VF = 0.2, AR = 1 (spherical; angle = 0); cube 3 at Location = 1, VF = 0.1, AR = 0.65, angle = 0; cube 4 at Location = 1.5, VF = 0.1, AR = 0.65, angle = 0. Case numbers can also be seen on the geometry.

To check if the printed cubes actually match the .stl designs, few extra random cases were printed. These extra cubes were cross-sectioned into halves and measurements were taken to check the dimensions of the inclusion if they match the .stl designs. They did perfectly.

For each of the 86 cases, the axial Young's modulus, E_{11} , is determined experimentally from the linear portion of the uniaxial compressive stress-strain curves obtained using a Tinius Olsen Hounsfield UTM machine. In line with

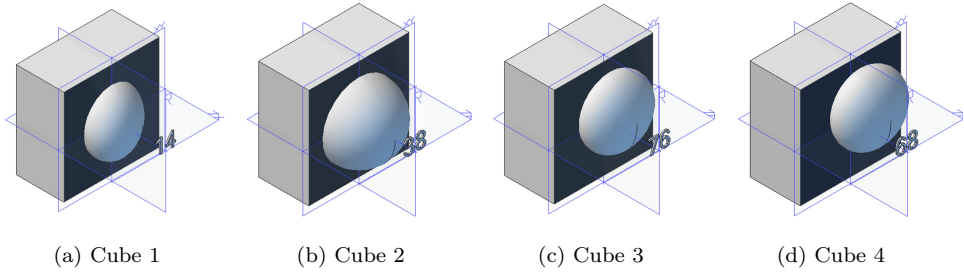


Fig. 3. Four test cases with different inclusion’s volume fractions, shapes, orientations, and locations in the matrix: (a) cube 1 at Location = 0, VF = 0.1, AR = 0.75, angle = 30; (b) cube 2 at Location = 0, VF = 0.2, AR = 1 (spherical; angle = 0); (c) cube 3 at Location = 1, VF = 0.1, AR = 0.65, angle = 0; (d) cube four at Location = 1.5, VF = 0.1, AR = 0.65, angle = 0; also shown is test case number.

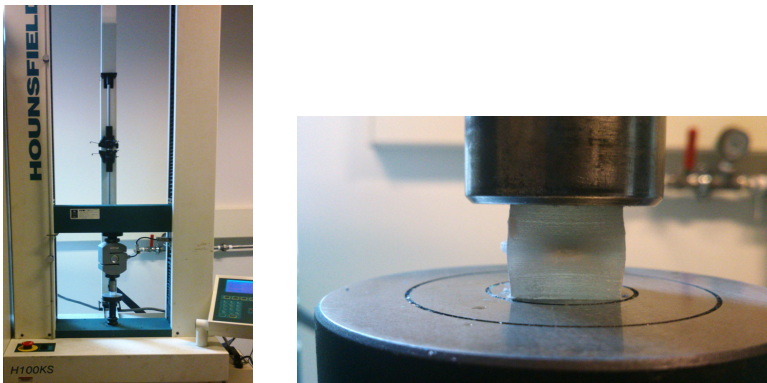


Fig. 4. Compression setup: (left) the Hounsfield UTM machine; (right) typical test in progress.

“ASTM D695-10 Standard Test Method for Compressive Properties of Rigid Plastics”, the +Z faces of the cubes were subjected to uniaxial compression at 1.3 mm/min feed rate. Force measurements are reported using load cell of 100 KN. Figure 4 shows photographs of the Hounsfield UTM machine setup: (left) compression test setup, and (right) typical test in progress.

Stress (MPa)–strain and load (N)–stroke (mm) plots for the 86 experiments are co-plotted in Figs. 5(a) and 5(b), respectively. The solid cube (with no inclusions) shows the highest stiffness as compared with other curves corresponding to inclusion-containing cubes. Stiffness values decrease with increasing volume fraction (each case plotted represents one value of volume fraction). This will be illustrated in detail in Fig. 9 (Sec. 6.2) when plotting normalized values of Young’s modulus versus volume fractions.

Figure 6 shows a plot of the numerical estimates of the normalized Young’s Modulus versus the experimentally measured Young’s Modulus at identical values

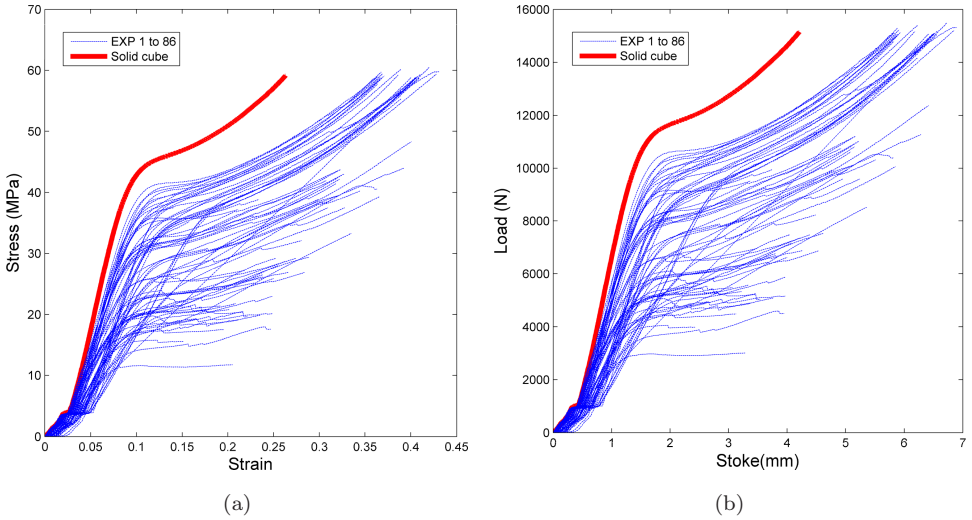


Fig. 5. Experimental compression results of 86 cases of cubes: (a) stress-strain, (b) load-stroke curves.

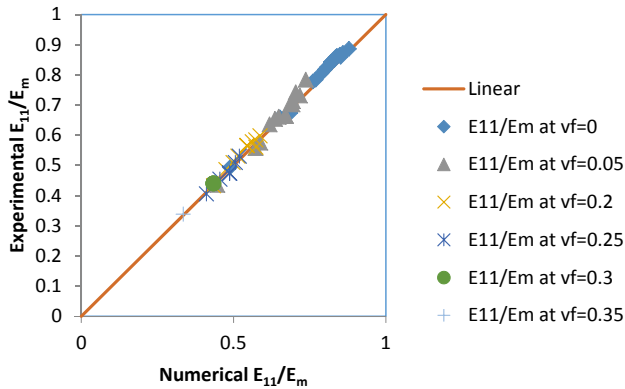


Fig. 6. Experimental results of the normalized Young's Modulus E_{11}/E_m plotted versus numerical results; inclusion volume fractions from 0 to 0.35.

of volume fractions (ranging from 0 to 0.35). The points cloud is located close to the $y = x$ line suggesting that experimental and numerical results are quite comparable which is indicative of the quality of the homogenization formulation.

5. Finite Element Method

For further validation of the homogenization scheme in Eq. (17), performed are finite element modeling simulations using DEFORM (from SFTC). The same .stl files generated using Cubify Design® software used to 3D print the cases are employed to

generate CAD files for FEM. Employed are the same 86 cases tested experimentally in Sec. 4 plus 28 additional cases raising the total number of FEM runs to 114 cases as follows:

- (1) Location 0 mm (0,0,0) (94 cases covering $VF = [0.1; 0.2; 0.25; 0.3; 0.35; 0.4; 0.5]$; $AR = [0.2; 0.4; 0.65; 0.75; 0.8; 0.9; 1]$; orientation = $[0^\circ; 30^\circ; 60^\circ; 90^\circ]$);
- (2) Location 1 mm (1,1,1) (12 cases covering $VF = [0.1; 0.2; 0.3; 0.35]$; $AR = [0.4; 0.65; 0.75; 0.9; 1]$; orientation = $[0^\circ]$)
- (3) Location 1.5 mm (1.5,1.5,1.5) (8 cases covering $VF = [0.1; 0.2]$; $AR = [0.4; 0.65; 0.75; 0.9; 1]$; orientation = $[0^\circ]$).

5.1. FEM simulation setup: meshing, materials, and boundary conditions

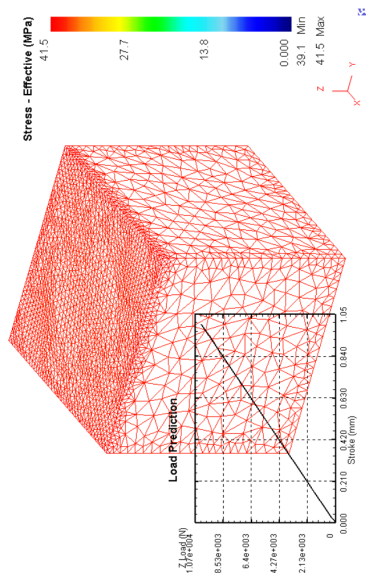
Tetrahedral elements are used to mesh the universe cube. Finer mesh is applied to the top surface of the cube at the contact with the upper UTM grip and around the inclusion resulting in a mesh with 31,109 elements. The maximum element size was 0.887 mm. The resulting mesh for solid cube is shown in Fig. 7 (top left) and typical inclusion-containing cube Fig. 7 (top right). Active re-meshing is utilized with a relative interference ratio of 0.7. The mechanical properties in Table 2 are assigned to the cube considered as elastic material. The $-z(-1)$ surface of the cube is defined as having fixed boundary displacement $uz = 0$. The $+z(+1)$ surface of the cube is defined to have a prescribed displacement rate of 1.3 mm/min as boundary condition of velocity with a speed as per “Compressive Properties of Rigid Plastics ASTM D695”. This boundary condition at the upper surface mimics the experimental upper rigid plate movement in the uniaxial compression test. Value was set to be less than 2 mm that represents the proportional linear elastic limit. The simulation time step is set as 0.001 sec/step based on the ratio relating the minimum model’s element size and the displacement rate.

5.2. FEM results

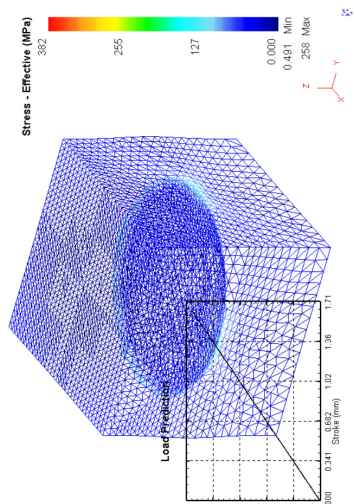
Elastic Young’s modulus values were extracted from the linear portions of the FEM-generated load versus stroke curves (runs terminated at yield). Figure 7 (inlaid within the plots are stress versus strain FEM results) shows representative load deformation curves generated using FEM for 4 representative runs:

- (a) Solid cube
- (c) case 1: cube with inclusion at location = 0, $VF = 0.1$, $AR = 0.2$, angle = 0° (with $E_{11}/E_m = 0.47$)
- (c) case 9: cube with inclusion at location = 0, $VF = 0.1$, $AR = 0.65$, angle = 0° (with $E_{11}/E_m = 0.78$)
- (d) case 27: cube with inclusion at location = 0, $VF = 0.2$, $AR = 0.65$, angle = 30° (with $E_{11}/E_m = 0.62$)

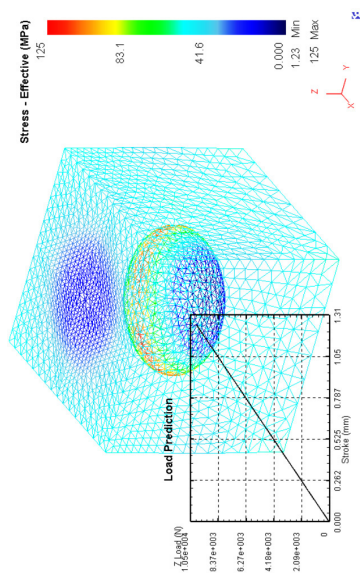
Full cube



Case 1



Case 9



Case 27

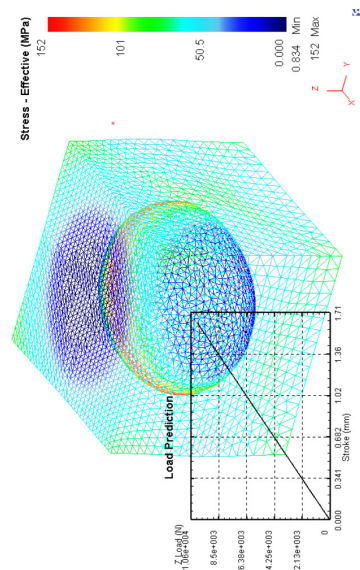


Fig. 7. Load versus stroke obtained using FEM for (top left) solid cube, (top right) case 1: cube with inclusion at location = 0, VF = 0.1, AR = 0.2, angle = 0 ($E_{11}/E_m = 0.47$), (bottom left) case 9: At location = 0, VF = 0.1, AR = 0.65, angle = 0 ($E_{11}/E_m = 0.78$), (bottom right) case 27: at location = 0, VF = 0.2, AR = 0.65, angle = 30 ($E_{11}/E_m = 0.62$).

6. Results and Discussion

The homogenization solution of Eq. (17) was automated using a custom MATLAB® code. Void’s volume fraction, aspect ratio, orientation, and location were considered as inputs for all 805 test cases listed above. A large subset (86) of those test cases were actually 3D printed. Figures 8–10 plot the values of normalized Young’s modulus with respect to that of the matrix, E_{11}/E_m , as determined from four sources: (1) NUM: numerical solutions of Eq. (17) using the MATLAB® homogenization code, (2) REG: SAS/STAT® derived non-linear regression expression (Eq. (19)), (3) FEM: DEFORM® results, and (4) experimental compression tests. The case of

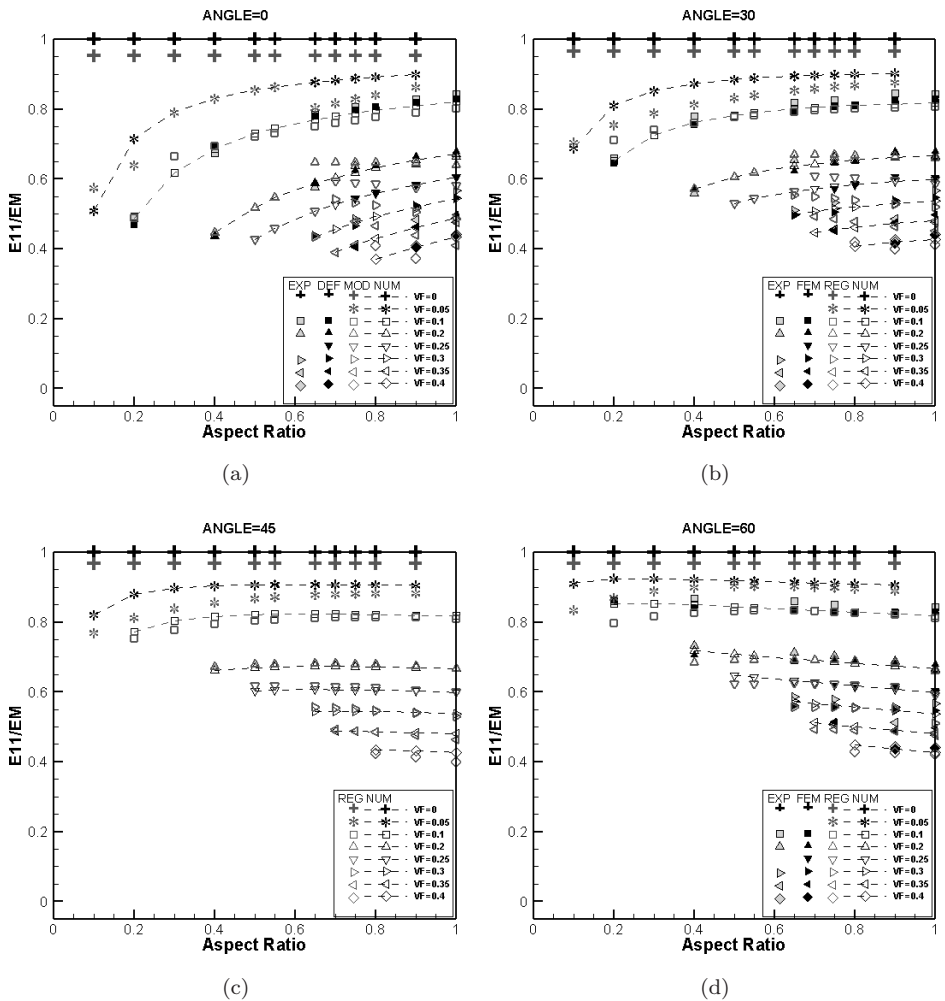


Fig. 8. E_{11}/E_m versus AR at fixed angle and varying VF. Angles (a) 0°, (b) 30°, (c) 45°, (d) 60°, (e) 90°; FEM: DEFORM® results, EXP: experimental results, REG: SAS results (Eq. (19)), NUM: numerical results (Eq. (17)).

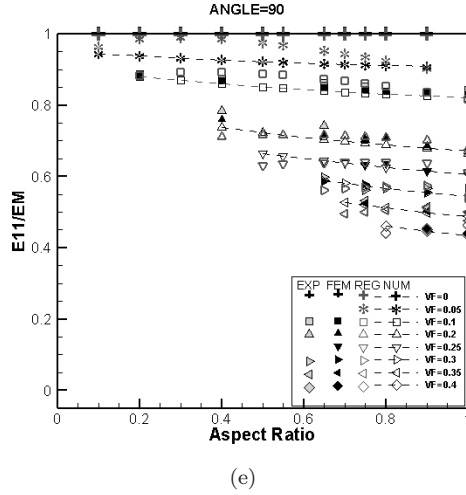


Fig. 8. (Continued)

an inclusion centered at $(0, 0, 0)$ is taken as control. Analysis of the results sorted by the inclusion's AR, VF, and orientation are stated hereafter.

6.1. Normalized longitudinal young's modulus versus aspect ratio

In Fig. 8, the normalized Young's modulus with respect to that of the matrix E_{11}/E_m , is plotted versus AR at selected values of AF and angle orientations ranging from 0° to 90° . All numerical, experimental, nonlinear regression expression and FEM results are in good agreement indicative of the accuracy of the developed homogenization methodology that estimates the combined effect of the four variables considered. The nonlinear regression model (covering all applicable variable ranges) mimics to a large degree the numerical code results suggesting that this model could be used in lieu of the computationally demanding MATLAB® code to determine the elastic properties of a matrix/inclusion system.

Results show that E_{11}/E_m increases with AR at angles ranging from $0-30^\circ$. However, E_{11}/E_m variation with AR is minimal at angle of 45° . E_{11}/E_m decreases with AR at angles ranging from $60-90^\circ$. Results are in agreement with Rouhi and Rais-Rohani [2011] where the axial Young's modulus E_{11}/E_m of the CNF enhanced vinyl ester increases as a function of CNF aspect ratio (at angle 0°) for different volume fractions using the Mori–Tanaka homogenization scheme. The effective longitudinal stiffness increases with aspect ratio for the CNT reinforced composites at various CNT volume fractions from 1% to 5% in Dong [2014]. In the report by Tandon and Weng [1984], the longitudinal Young's modulus E_{11} of unidirectionally aligned composites at angle 0° increase with increasing aspect ratio. For volume fraction = 0.05, the SAS regression model estimates show some deviation from those of the numerical model (Eq. (18)).

6.2. Normalized longitudinal Young's modulus versus volume fraction

In Fig. 9, the normalized Young's modulus values with respect to that of the matrix E_{11}/E_m are plotted versus VF (at fixed select values of AR and for several angles). Numerical, experimental, and FEM results are co-plotted as shown in Fig. 9 for aspect ratios: (a) 0.2, (b) 0.4, (c) 0.65, (d) 0.75, (e) 0.9, and (f) 1. For comparison purposes, 2 additional sets of results are co-plotted corresponding to the mixture rule as per Voigt upper limit (VUL) [Voigt, 1887] and the Hashin-Shtrikman lower limit (HSSL) (see Hashin and Shtrikman [1963]). Results show that the normalized Young's modulus decreases with VF within the upper and lower mixture rule limits.

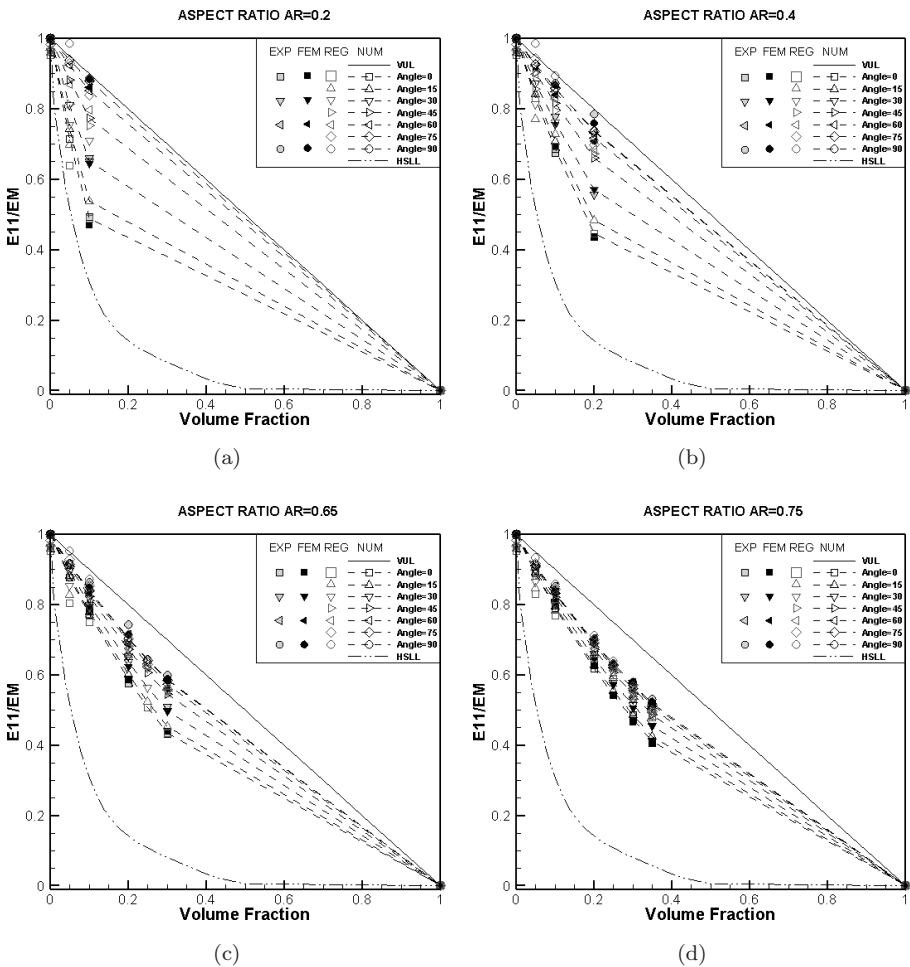


Fig. 9. E_{11}/E_m versus VF at fixed AR and various angles; Aspect ratio (a) 0.2, (b) 0.4, (c) 0.65, (d) 0.75, (e) 0.9, (f) 1; FEM: DEFORM® results, EXP: experimental results, REG: SAS results (Eq. (19)), NUM: numerical results (Eq. (17)).

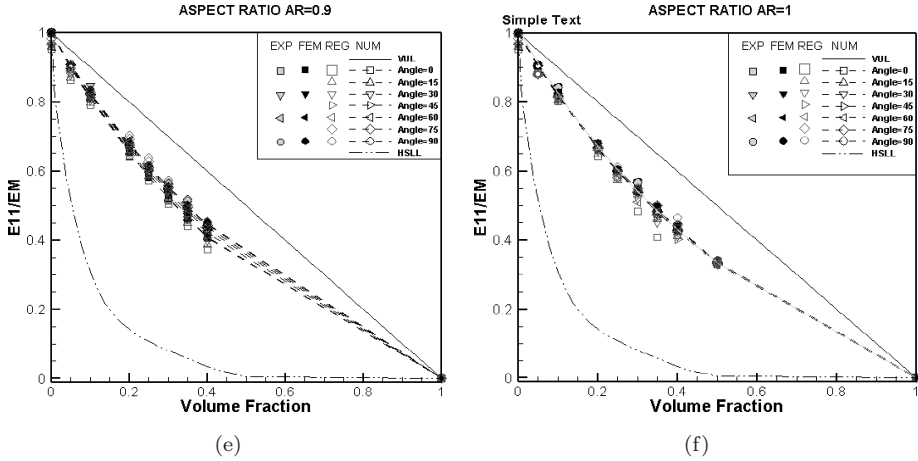


Fig. 9. (Continued)

As AR increases, the curves at each angle converge meaning that the closer AR is to 1 (ellipsoid approaches a sphere) the effect of orientation becomes small. With AR increasing, E_{11}/E_m versus VF becomes closer to VUL, in agreement with the findings by Tandon and Weng [1984].

6.3. Normalized longitudinal Young's modulus versus orientation angle

Plotted in Fig. 10 are normalized Young's modulus values with respect to that of the matrix, E_{11}/E_m , versus angle at fixed AR values for varying values of VF. Values of

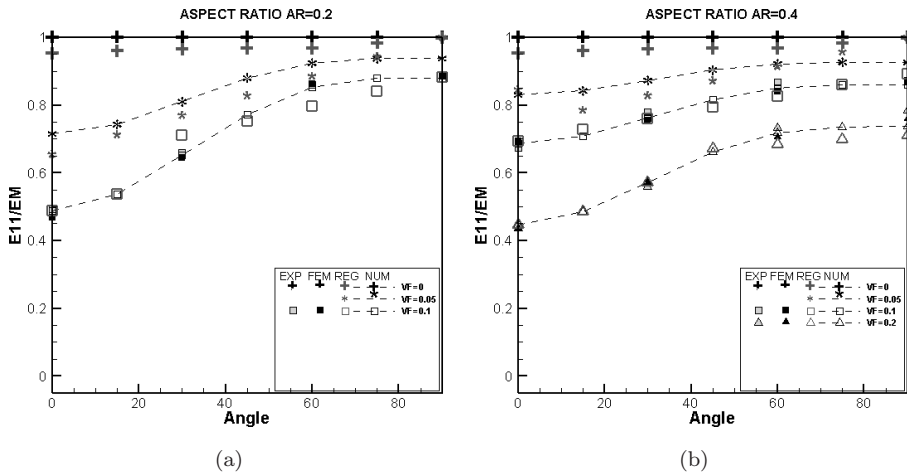


Fig. 10. E_{11}/E_m versus angle at fixed AR and various VF. Aspect ratio (a) AR = 0.2, (b) AR = 0.4, (c) AR = 0.65, (d) AR = 0.75, (e) AR = 0.9, (f) AR = 1. (FEM: DEFORM® results, EXP: experimental results, REG: SAS results (Eq. (19)), NUM: numerical results (Eq. (17))).

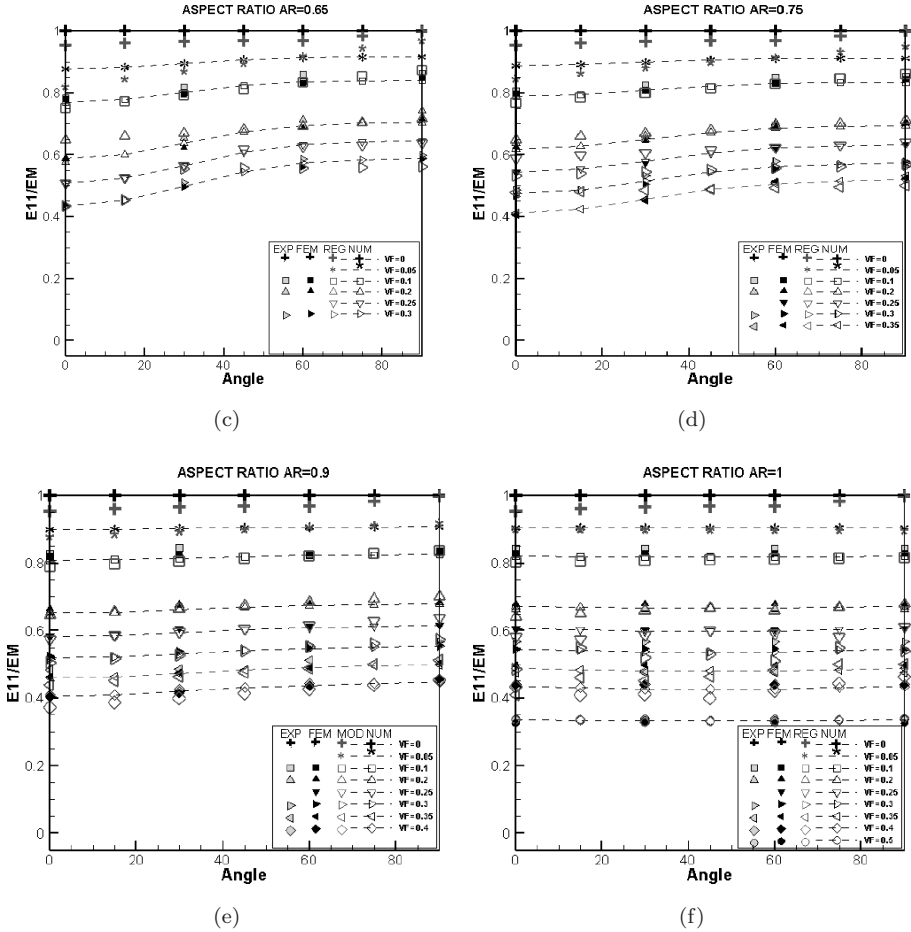


Fig. 10. (Continued)

E_{11}/E_m versus angle increase significantly with angle. As AR approaches unity, this trend becomes less dramatic, similar to observations by Johannesson and Pedersen [1998]. Results are in line with those reported by Rouhi and Rais-Rohani [2011] where normalized effective stiffness values decrease with CNT orientation angle. Kushch and Sevostianov [2004] reported that the normalized stiffness modulus, C_{33} , is reduced by up to two times as θ varies from 0° to $\pi/2$.

6.4. Normalized Young's modulus versus location

It is verified numerically, experimentally, and with FEM that the effect of inclusion location inside the cube (position) on cube stiffness is not significant. The maximum percentage difference obtained between location 0 and locations (1, 1, 1) and (1.5, 1.5, 1.5) is 0.88%

7. Summary and Conclusions

For a single inclusion in a finite solid domain, a homogenization formulation is developed to calculate the domain's effective stiffness tensor due to the combined effect of the inclusion's four geometric attributes: size (volume fraction), shape (aspect ratio), orientation, and location. The developed formulation is based on the Modified Mori–Tanaka method combined with the dual-eigenstrain method taking into account all four considered variables in one formulation. An Eshelby tensor dependent on the inclusion's shape and position is deduced.

The formulation is solved, experimentally corroborated, and FEM-validated for numerous cases of inclusion with widely ranging attributes. The findings suggest that normalized longitudinal Young's modulus, E_{11}/E_m , values:

- increase with AR at angles in the range 0° – 30° , at 45° E_{11}/E_m is almost constant with AR, and decreases with AR at angles 60 – 90° .
- decrease with increasing inclusion's volume fraction.
- for fixed AR, increase significantly with increasing angle (but the increase becomes less profound as AR approaches unity).
- are practically independent of location of the inclusion.

Given the complexity and time required to run a complex MATLAB® code, it was also desired to develop a relatively simple equation capable of returning normalized axial Young's modulus of all four combined inclusion variables. This was accomplished via a nonlinear regression modeling module in SAS/STAT® software that fit the numerical solutions of all considered cases into a relatively simple equation in all four variables (Eq. (19)) which fairly accurately returns the composite stiffness. Future works include extending the numerical approach to account for the effect of multiple inclusions in the same cube domain.

Acknowledgments

This work was made possible by the support of the Lebanese National Council for Scientific Research (CNRS) Award Number 103087. The authors also wish to acknowledge the financial support of the University Research Board at AUB.

References

- Anouar, B., Larbi, S., Luc, D. and Liu, W. K. [2010] "Yield design homogenization method for compaction of monosized spherical powders," *International Journal of Applied Mechanics* **2**(3), 457–488.
- Dong, C. [2014] "Mechanical and thermo-mechanical properties of carbon nanotube reinforced composites," *International Journal of Smart and Nano Materials* **5**(1), 44–58.
- Eshelby, J. D. [1957] "The determination of the elastic field of an ellipsoidal inclusion, and related problems," *Proceedings of the Royal Society of London A: Mathematical, Physical and Engineering Sciences, The Royal Society* **241**, 376–396.

- Hashin, Z. and Shtrikman, S. [1963] “A variational approach to the theory of the elastic behaviour of multiphase materials,” *Journal of the Mechanics and Physics of Solids* **11**(2), 127–140.
- Huang, Y., Hu, K. and Chandra, A. [1994] “A self-consistent mechanics method for solids containing inclusions and a general distribution of cracks,” *Acta Mechanica* **105**(1–4), 69–84.
- Johannesson, B. and Pedersen, O. B. [1998] “Analytical determination of the average Eshelby tensor for transversely isotropic fiber orientation distributions,” *Acta Materialia* **46**(9), 3165–3173.
- Ju, J. and Sun, L. [1999] “A novel formulation for the exterior-point Eshelby’s tensor of an ellipsoidal inclusion,” *Journal of Applied Mechanics* **66**(2), 570–574.
- Ju, J. and Sun, L. [2001] “Effective elastoplastic behavior of metal matrix composites containing randomly located aligned spheroidal inhomogeneities. Part I: micromechanics-based formulation,” *International Journal of Solids and Structures* **38**(2), 183–201.
- Koay, C. G. [2009] “On the six-dimensional orthogonal tensor representation of the rotation in three dimensions: A simplified approach,” *Mechanics of Materials* **41**(8), 951–953.
- Krzehchovskii, P. [1979] “Determination of elastic and strength characteristics of composites based on hollow spherical inclusions,” *Problemy Prochnosti* **3**, 37–40.
- Kushch, V. and Sevostianov, I. [2004] “Effective elastic properties of the particulate composite with transversely isotropic phases,” *International Journal of Solids and Structures* **41**(3), 885–906.
- Li, S., Sauer, R. A. and Wang, G. [2007a] “The Eshelby tensors in a finite spherical domain — Part I: Theoretical formulations,” *Journal of Applied Mechanics* **74**(4), 770–783.
- Li, S., Wang, G. and Sauer, R. A. [2007b] “The Eshelby tensors in a finite spherical domain — Part II: Applications to homogenization,” *Journal of Applied Mechanics*, **74**(4), 784–797.
- Lu, P., Leong, Y., Pallathadka, P. and He, C. [2013] “Effective moduli of nanoparticle reinforced composites considering interphase effect by extended double-inclusion model—Theory and explicit expressions,” *International Journal of Engineering Science* **73**, 33–55.
- Ma, H. and Gao, X. [2014] “A new homogenization method based on a simplified strain gradient elasticity theory,” *Acta Mechanica* **225**(4–5), 1075–1091.
- Marklund, E., Varna, J., Neagu, R. C. and Gamstedt, E. K. [2008] “Stiffness of aligned wood fiber composites: effect of microstructure and phase properties,” *Journal of Composite Materials* **42**(22), 2377–2405.
- Mori, T. and Tanaka, K. [1973] “Average stress in matrix and average elastic energy of materials with misfitting inclusions,” *Acta Metallurgica* **21**(3), 571–574.
- Rouhi, M. and Rais-Rohani, M. [2011] “Modeling and uncertainty quantification of nanofiber enhanced polymer composite materials with functionally graded interphase properties,” *52nd AIAA/ASME/ASCE/AHS/ASC Structures, Structural Dynamics and Materials Conference*. American Institute of Aeronautics and Astronautics (AIAA) (Denver, Colorado), p. 1924.
- Sun, Xiangkun, Changwei Zhou, Mohamed Ichchou, Jean-Pierre Lainé and Abdel-Malek Zine1 [2017] “Multi-scale homogenization of transversal waves in periodic composite beams,” *International Journal of Applied Mechanics* **9**, 1750039.
- Tandon, G. and Weng, G. [1984] “The effect of aspect ratio of inclusions on the elastic properties of unidirectionally aligned composites,” *Polymer Composites* **5**(4), 327–333.

- Timoshenko, S., Timoshenko, S. and Goodier, J. [1951] *Theory of Elasticity*, by S. Timoshenko and J. N. Goodier (McGraw-Hill book Company, Pennsylvania).
- Voigt, W. [1887] "Theoretische Studien über die Elasticitätsverhältnisse der krystalle (Theoretical studies on the elasticity ratios of crystals)," *Göttingen Dieterichsche Verlags-Uchhandlung* **34**, 100.
- Weng, G. [1984] "Some elastic properties of reinforced solids, with special reference to isotropic ones containing spherical inclusions," *International Journal of Engineering Science* **22**(7), 845–856.
- Yan, Z., Zhang, J., Ye, W. and Yu, T. [2010] "Numerical characterization of porous solids and performance evaluation of theoretical models via the precorrected-FFT accelerated BEM," *Computer Modeling in Engineering and Sciences (CMES)* **55**(1), 33.
- Yu, W. and Tang, T. [2009] "Variational asymptotic method for unit cell homogenization," *Advances in Mathematical Modeling and Experimental Methods for Materials and Structures* (Springer, Newyork), pp. 117–130.
- Zhong, Z., and Meguid, S. [1996] "On the eigenstrain problem of a spherical inclusion with an imperfectly bonded interface," *Journal of Applied Mechanics* **63**(4), 877–883.
- Zhong, Z. and Meguid, S. [1999] "On the imperfectly bonded spherical inclusion problem," *Journal of Applied Mechanics* **66**(4), 839–846.